Applied Mathematics and Computation 439 (2023) 127587

Contents lists available at ScienceDirect

Applied Mathematics and Computation

journal homepage: www.elsevier.com/locate/amc

Well-balanced numerical method for atmospheric flow equations with gravity

Alina Chertock[a], Alexander Kurganov[b,*], Tong Wu[c], Jun Yan[a]

[a] Department of Mathematics, North Carolina State University, Raleigh, NC 27695, USA
[b] Department of Mathematics, SUSTech International Center for Mathematics and Guangdong Provincial Key Laboratory of Computational Science and Material Design, Southern University of Science and Technology, Shenzhen 518055, China
[c] Department of Mathematics, University of Texas, San Antonio, TX 78249, USA

ARTICLE INFO

Article history:
Received 28 June 2022
Revised 2 September 2022
Accepted 26 September 2022
Available online 20 October 2022

MSC:
76M12
65M08
86-08
35L65

Keywords:
Atmospheric flow equations with gravity
Well-balanced central-upwind scheme
Equilibrium variables
Quadrilateral mesh
Irregular domains

ABSTRACT

We are interested in simulating gravitationally stratified atmospheric flows governed by the compressible Euler equations in irregular domains. In such simulations, one of the challenges arises when the computations are conducted on a Cartesian grid. The use of regular rectangular grids that intersect with the irregular boundaries leads to the generation of arbitrarily small and highly distorted computational cells adjacent to the boundaries of the domain. The appearance of such cells may affect both the stability and efficiency of the numerical method and therefore require special attention.

In order to overcome this difficulty, we introduce a structured quadrilateral mesh, which is designed for the irregular domain at hand, and solve the studied atmospheric flow equations using a second-order central-upwind scheme. In addition, the resulting numerical method is developed to provide a well-balanced discretization of the underlying system. The latter is achieved by rewriting the governing equations in terms of equilibrium variables representing perturbations of the known background equilibrium state. The proposed method is tested in a number of numerical experiments, including the buoyant bubble rising and interacting with an (zeppelin) obstacle and the Lee wave generation due to topography. The obtained numerical results demonstrate high resolution and robustness of the proposed computational approach.

1. Introduction

Gravitationally stratified flows in a compressible medium are widely used in atmospheric models to predict weather and climate. These models are typically characterized as variants of the compressible Euler equations with gravity. Here, we focus on studying the following two-dimensional (2-D) system proposed in Klein et al. [18]:

$$\begin{cases} \rho_t + (\rho u)_x + (\rho v)_y = 0, \\ (\rho u)_t + (\rho u^2 + p)_x + (\rho uv)_y = 0, \\ (\rho v)_t + (\rho vu)_x + (\rho v^2 + p)_y = -\rho g, \\ (\rho\theta)_t + (\rho\theta u)_x + (\rho\theta v)_y = 0, \end{cases} \tag{1.1}$$

* Corresponding author.
E-mail addresses: chertock@math.ncsu.edu (A. Chertock), alexander@sustech.edu.cn (A. Kurganov), Tong.wu@utsa.edu (T. Wu), jyan9@ncsu.edu (J. Yan).

https://doi.org/10.1016/j.amc.2022.127587
0096-3003/

where x and y are spatial variables, t is the time, $\rho(x,y,t)$, $u(x,y,t)$, $v(x,y,t)$ and $\theta(x,y,t)$ are the density, horizontal, vertical velocities and potential temperature, respectively, and g is the acceleration due to gravity. The air flow is assumed to be an ideal gas satisfying the equation of state:

$$p = (\rho\theta)^{\gamma}, \tag{1.2}$$

where p is the pressure and $\gamma = 1.4$ is the specific heat ratio.

Time-independent (steady-state or equilibrium) solutions of the system (1.1) play an important role as many atmospheric phenomena are described by small perturbations of the steady states. In particular, one of the physically relevant equilibria is the hydrostatic one:

$$u = v \equiv 0, \quad p_x \equiv 0, \quad p_y = -\rho g. \tag{1.3}$$

Capturing small perturbations of (1.3) numerically is a challenging task since at a large scale or on a coarse grid the magnitude of such perturbations may be smaller than the size of truncation errors. Obviously, the truncation errors may be reduced by refining the computational mesh, but this would make the numerical simulations very inefficient or even impractical. Therefore, the goal is to develop *well-balanced* numerical methods, which are capable of preserving the underlying steady states exactly, that is, without any truncation errors. Several well-balanced numerical methods capable of exactly preserving hydrostatic steady-states solutions have been proposed; see, e.g., Botta et al. [3], Chertock et al. [5], Gaburro et al. [7], Gatti-Bono and Colella [9], Ghosh and Constantinescu [10], Grosheintz-Laval and Käppeli [15], Käppeli and Mishra [17], Klein et al. [18], Klingenberg et al. [19], LeVeque [26], Wu and Xing [32], Xing and Shu [33], Yelash et al. [34] and references therein.

Another challenge one faces while numerically solving the system (1.1) and (1.2) is to capture its solutions near irregular boundaries. Several techniques were proposed to address this problem. In the older works, the terrain-following coordinate approach was widely used in atmospheric simulations; see, e.g., Gal-Chen and Somerville [8], Phillips [28], Simmons and Burridge [30]. It normalizes the vertical coordinate by the fluid depth to incorporate the topography of domains into the studied models. However, this approach typically leads to significant truncation errors near boundaries, especially when the flow contains steep gradients; see, e.g., Janji [16], Sundqvist [31]. Alternatively, one may use Cartesian-grid based methods, which are relatively simple, but suffer from the appearance of arbitrarily small and highly distorted cells adjacent to the boundaries of the domain. Such cut cells may lead to stability and efficiency issues for numerical methods and therefore require special techniques; see, e.g., Berger and Helzel [1], Brady and Livescu [4], Gatti-Bono and Colella [9], Gokhale et al. [12], Klein et al. [18], Mittal and Iaccarino [27] and references therein. Triangular, quadrilateral and cell-vertex polygonal meshes can also be used to conduct simulations in domains with irregular boundaries. It should be observed that unstructured meshes with different polygons can accurately represent irregular boundaries and thus provide with a flexible tool to handle regions with steep topographic gradients.

In this paper, we develop a well-balanced method for the system (1.1) and (1.2) in two steps. We first follow [2,11,21,34] and rewrite the studied system in terms of the perturbation variables and thus ensure that the resulting method is well-balanced in the sense that it is capable of exactly preserving a known background equilibrium state. We then introduce a structured quadrilateral mesh, which is specifically designed for every considered irregular domain. Finally, the rewritten system is numerically integrated using the second-order semi-discrete central-upwind scheme, which was introduced in Kurganov and Lin [20], Kurganov et al. [22], Kurganov and Tadmor [25] as a robust and highly accurate "black-box solver" for general multidimensional system of hyperbolic conservation and balance laws (including the compressible Euler equations with gravitation [5]) on Cartesian grids, and then extended to structured and unstructured quadrilateral meshes in Kurganov et al. [23,24], Shirkhani et al. [29].

The paper is organized as follows. In Section 2, we introduce the perturbation variables and use them to rewrite the system (1.1) and (1.2) in the form suitable for the development of well-balanced methods. We also briefly discuss the implementation of the second-order semi-discrete central-upwind scheme on structured quadrilateral meshes for the rewritten system. In Section 3, we show how to design appropriate quadrilateral meshes on three numerical examples and demonstrate high resolution and robustness of the proposed numerical method.

2. Model description and numerical method

In this section, we follow the idea from Bispen et al. [2], Giraldo et al. [11], Kurganov et al. [21], Yelash et al. [34] and achieve the well-balanced property of proposed numerical method by rewriting the system (1.1) and (1.2) in terms of the perturbation variables. To this end, we first denote the known background equilibrium state satisfying (1.3) by $\rho_s(y)$ and $p_s(y)$ with the corresponding potential temperature $\theta_s(y) = [p_s(y)]^{1/\gamma}/\rho_s(y)$, and introduce the perturbation variables ρ', u', v' and θ' so that

$$\rho = \rho_s + \rho', \quad u = u', \quad v = v', \quad \theta = \theta_s + \theta', \quad p' = \Big[(\rho_s + \rho')(\theta_s + \theta')\Big]^{\gamma} - p_s. \tag{2.1}$$

where p' is obtained from the equation of state (1.2). We then rewrite the system (1.1) in the following form:

$$\begin{cases} \rho'_t + (\rho u')_x + (\rho v')_y = 0, \\ (\rho u')_t + [\rho (u')^2 + p']_x + (\rho u' v') = 0, \\ (\rho v')_t + (\rho v' u')_x + [\rho (v')^2 + p']_y = -\rho' g, \\ (\rho\theta)_t + (\rho\theta u')_x + (\rho\theta v')_y = 0. \end{cases} \tag{2.2}$$

The main advantage of the system (2.2) over its original counterpart (1.1) is that when the solution is at the steady state, the perturbation variables vanish and this makes it easy to design a well-balanced numerical method. In this paper, we use the second-order semi-discrete central-upwind scheme as it is described in Kurganov et al. [24] with the only exception that the piecewise linear reconstruction is now performed not for the conservative variables $\boldsymbol{U} := (\rho', \rho u', \rho v', \rho\theta)$, but for the perturbation variables $\boldsymbol{U}' := (\rho', u', v', \theta')$, which remain constant (zero) at the steady state (1.3).

The central-upwind scheme can be briefly described as follows. Let us assume that the computational domain is covered with a structured quadrilateral mesh consisting of cells $C_{j,k}$ with vertices $(x_{j-\frac{1}{2},k-\frac{1}{2}}, y_{j-\frac{1}{2},k-\frac{1}{2}})$, $(x_{j-\frac{1}{2},k+\frac{1}{2}}, y_{j-\frac{1}{2},k+\frac{1}{2}})$, $(x_{j+\frac{1}{2},k-\frac{1}{2}}, y_{j+\frac{1}{2},k-\frac{1}{2}})$ and $(x_{j+\frac{1}{2},k+\frac{1}{2}}, y_{j+\frac{1}{2},k+\frac{1}{2}})$, the center of mass $(x_{j,k}, y_{j,k})$, and area $|C_{j,k}|$. We also assume that the computed cell averages,

$$\bar{\boldsymbol{U}}_{j,k}(t) \approx \frac{1}{|C_{j,k}|} \iint\limits_{C_{j,k}} \boldsymbol{U}(x,y,t)\,\mathrm{d}x\,\mathrm{d}y.$$

are available at a certain time level t and we use them to approximate the corresponding point values of $\boldsymbol{U}'$ at the center of mass of cell $C_{j,k}$:

$$\rho'_{j,k} = \bar{\rho}'_{j,k}, \quad u'_{j,k} = \frac{(\bar{\rho u'})_{j,k}}{\rho_{j,k}}, \quad v'_{j,k} = \frac{(\bar{\rho v'})_{j,k}}{\rho_{j,k}}, \quad \theta'_{j,k} = \frac{(\bar{\rho\theta'})_{j,k}}{\rho_{j,k}} - \theta_s(y_{j,k}).$$

Here, $\rho_{j,k} = \bar{\rho}'_{j,k} + \rho_s(y_{j,k})$ and the dependence of the indexed quantities on t has been omitted for the sake of brevity.

Equipped with the point values $\left\{\boldsymbol{U}'_{j,k}\right\}$, we obtain the point values of $\boldsymbol{U}'$ at the cell interfaces using the piecewise linear reconstruction consisting of the pieces

$$\boldsymbol{U}'_{j,k} + (\boldsymbol{U}'_x)_{j,k}(x - x_{j,k}) + (\boldsymbol{U}'_y)_{j,k}(y - y_{j,k}), \quad (x,y) \in C_{j,k}.$$

The slopes $(\boldsymbol{U}'_x)_{j,k}$ and $(\boldsymbol{U}'_y)_{j,k}$ here are computed using a nonlinear minmod-type limiter proposed in Kurganov et al. [24]; see Kurganov et al. [24, §2.2] for details. We then use (2.1) to obtain all of the point values of $\boldsymbol{U}$ at the cell interfaces required in the computation of the central-upwind numerical fluxes $\boldsymbol{H}_{j\pm\frac{1}{2},k}$ and $\boldsymbol{H}_{j,k\pm\frac{1}{2}}$ across the cell interfaces between $C_{j,k}$ and its four neighboring cells; the details on the computation of these fluxes can be found in Kurganov et al. [24, §2.2]. The solution is then evolved in time by solving the following system of ODEs:

$$\frac{\mathrm{d}}{\mathrm{d}t}\bar{\boldsymbol{U}}_{j,k} = -\frac{1}{|C_{j,k}|}\left(\boldsymbol{H}_{j+\frac{1}{2},k} - \boldsymbol{H}_{j-\frac{1}{2},k} + \boldsymbol{H}_{j,k+\frac{1}{2}} - \boldsymbol{H}_{j,k-\frac{1}{2}}\right) + \bar{\boldsymbol{S}}_{j,k}, \tag{2.3}$$

where $\bar{\boldsymbol{S}}_{j,k} = (0, 0, -\bar{\rho}'_{j,k} g, 0)^\top$ is the approximation of the source cell average obtained using the midpoint rule. Finally, the system (2.3) is integrated using the three-stage third-order strong stability-preserving Runge–Kutta (SSP-RK3) method; see, e.g., Gottlieb et al. [13,14].

Remark 2.1. Notice that the gravitational source term on the right-hand side of (2.3) vanishes at the steady state (1.3). Therefore, approximating its cell averages using the midpoint rule leads to a well-balanced discretization.

Remark 2.2. We emphasize that the method presented in this section can be applied not only to the studied system (1.1), but to many different 2-D systems of balance laws for which the background state is known. This is due to the fact that the central-upwind scheme can be applied as a "black-box" solver as long as the one-sided local speeds of propagation, which are based on the largest and smallest eigenvalues of the Jacobian of the flux in the direction perpendicular to the cell interface, are available (this is the case for the system (2.2) studied in this paper).

3. Numerical examples

In this section, we demonstrate the performance of the proposed well-balanced central-upwind scheme on three numerical examples. In all of the experiments, we take the minmod-type reconstruction parameter $\psi = 1.3$; see Kurganov et al. [24, Equation (2.9)].

3.1. Example 1 (convergence test)

In the first example, we experimentally check the accuracy of the proposed method. We take $g = 1$.

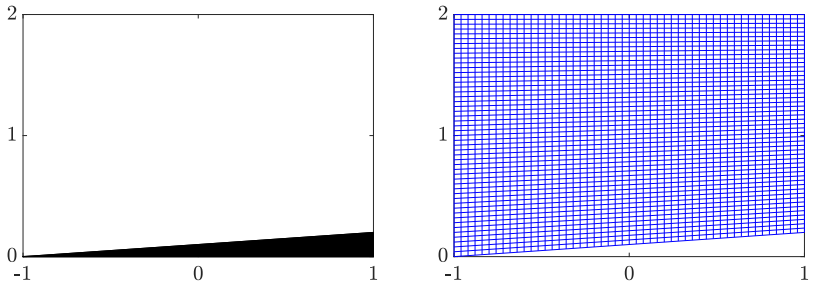

Fig. 3.1. Example 1: Computational domain (left) and structured quadrilateral mesh (right).

Table 3.1
Example 1: Experimental convergence rates in the L^1-norm.

N	$\Delta\rho_N$	Rate	$\Delta(\rho u)_N$	Rate	$\Delta(\rho v)_N$	Rate	$\Delta(\rho\theta)_N$	Rate
100	0.9288E−4	–	0.9354E−5	–	0.1236E−4	–	0.5476E−4	–
200	0.2506E−4	1.89	0.3488E−5	1.42	0.0381E−4	1.70	0.1479E−4	1.89
400	0.0639E−4	1.97	0.0875E−5	2.00	0.0092E−4	2.05	0.0354E−4	2.06
800	0.0162E−4	1.98	0.0210E−5	2.06	0.0024E−4	1.96	0.0089E−4	1.99

3.1.1. Problem settings

We take a relatively simple computational domain $\{(x,y) : -1 \le x \le 1,\ 0.1(x+1) \le y \le 2\}$; see Fig. 3.1 (left).

The steady-state solution satisfying (1.3) and (1.2) is made of one layer atmosphere and given by

$$\theta_s(y) = e^{y/4}, \quad p_s(y) = \left(1 + \frac{8}{7}\left(e^{-y/4} - 1\right)\right)^{7/2}, \quad \rho_s(y) = \frac{[p_s(y)]^{5/7}}{\theta_s(y)}.$$

We introduce a small perturbation in the potential temperature only,

$$\theta'(x,y,0) = 0.01e^{-100(x^2+(y-0.5)^2)},$$

while setting

$$u'(x,y,0) = v'(x,y,0) \equiv 0, \quad \rho'(x,y,0) \equiv 0, \quad p'(x,y,0) \equiv 0.$$

In addition, solid wall boundary conditions are applied on all of the four sides of the computational domain.

3.1.2. Mesh generation

Structured quadrilateral mesh can be easily generated in this example by equally spacing left and right boundaries for the horizontal distance and top and bottom boundaries for vertical distances; see Fig. 3.1 (right). Then, the constructed cell vertices are

$$\begin{cases} x_{j+\frac{1}{2},k+\frac{1}{2}} = -1 + \frac{2j}{M}, \\ y_{j+\frac{1}{2},k+\frac{1}{2}} = \left(1 - \frac{k}{N}\right)0.1\left(x_{j+\frac{1}{2},\frac{1}{2}} + 1\right) + \frac{2k}{N}, \end{cases} \quad j = 0,\ldots,M, \quad k = 0,\ldots,N.$$

3.1.3. Results

We measure the experimental convergence rates using the numerical solutions computed with $M = N$ for $N = 50$, 100, 200, 400 and 800 at time $t = 0.1$. The convergence rates are calculated using the numerical solutions on successively refined grids. For example, let us denote by ρ_N the density computed using the $N \times N$ mesh. Then the estimated convergence rate for the density field is

$$\text{Rate} \approx \log_2\left(\frac{\|\Delta\rho_{N/2}\|_1}{\|\Delta\rho_N\|_1}\right), \quad \Delta\rho_N := \|\rho_N - \rho_{N/2}\|_1.$$

The corresponding convergence rates for the other fields can be obtained similarly.

The results of the mesh refinement study are reported in Table 1. As one can see, the proposed method achieves the expected second order of accuracy.

3.2. Example 2 (zeppelin test)

In this test, we consider an example from Durran [6], Klein et al. [18], in which the hot air is propagating upward and flows around a stationary suspended zeppelin. We take $g = 1.14$.

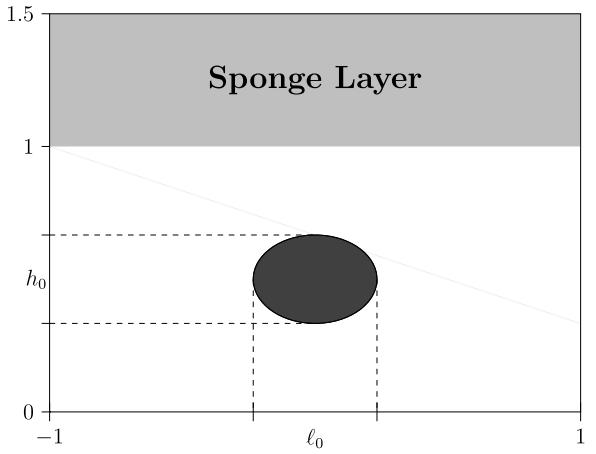

Fig. 3.2. Example 2: Computational domain.

3.2.1. Problem settings

We solve the studied atmospheric flow equations in a vertically stratified atmosphere with a stationary elliptic obstacle suspended in the air. The computational domain is presented in Fig. 3.2. The boundary of the obstacle is given by

$$\frac{x^2}{\ell_0^2}+\frac{(y-0.5)^2}{h_0^2}=\frac{1}{4},$$

where $h_0=0.333$ is the height and $\ell_0=0.466$ is the length of the zeppelin.

In order to minimize gravity wave reflection from the top of the domain, we use the highlighted upper part of the computational domain as a sponge layer; see Fig. 3.2. To this end, we replace the computed solution at every stage of the SSP-RK3 method with the following relaxed values:

$$\bar{\boldsymbol{U}}^{\text{relax}}_{j,k}=\bar{\boldsymbol{U}}^{0}_{j,k}+\frac{1}{1+\frac{\Delta t}{10}\hat{y}}\Big(\bar{\boldsymbol{U}}_{j,k}-\bar{\boldsymbol{U}}^{0}_{j,k}\Big),$$

where $\bar{\boldsymbol{U}}^{0}_{j,k}$ are the initial data and $\hat{y}:=\max\big(y_{j,k}-1,0\big)$ is the distance from the center of mass $(x_{j,k},y_{j,k})$ of cell $C_{j,k}$ to the non-sponge part of the computational domain.

In this example, the steady-state solution satisfying (1.3) and (1.2) is

$$\theta_s(y)\equiv 1,\quad p_s(y)=\Big(1-\frac{2}{7}gy\Big)^{7/2},\quad \rho_s(y)=\Big(1-\frac{2}{7}gy\Big)^{5/2}.$$

We introduce the initial perturbations in the potential temperature and pressure so that

$$\theta'(x,y,0)=\theta_B\cos^2\left(\frac{\pi r}{2}\right),\quad p'(x,y,0)=p_s(y)\left(\left[1+\theta_B\cos^2\left(\frac{\pi r}{2}\right)\right]^{7/5}-1\right),\tag{3.1}$$

while setting

$$u'(x,y,0)=v'(x,y,0)\equiv 0,\quad \rho'(x,y,0)\equiv 0.$$

In (3.1), $r=\min\Big\{\frac{1}{R_B}\sqrt{(x-x_B)^2+(y-y_B)^2},1\Big\}$, with $R_B=0.15$, $(x_B,y_B)=(-0.23,0.2)$ and $\theta_B=0.0333$ being the radius, center and magnitude of the initial perturbation.

In addition, solid wall conditions are applied on the boundary of the zeppelin and on the top and the bottom of the computational domain, while periodic boundary conditions are implemented on the horizontal domain edges.

3.2.2. Mesh generation

The structured quadrilateral mesh we have used in this example is presented in Fig. 3.3.

This mesh is constructed as follows. We first consider the mesh in the non-sponge part of the computational domain in $[-1,1]\times[0,1]$ and introduce the cell vertices there:

$$\Big\{\big(x_{j+\frac12,k+\frac12},y_{j+\frac12,k+\frac12}\big)\Big\},\quad j=-M,\ldots,M,\quad k=-N,\ldots,N.$$

Our goal is to make the generated mesh structured and avoid flat angles in the mesh cells. The difficulty is related to the presence of the elliptic obstacle inside the domain, which we split into several simpler parts using the following four symmetric points on the boundary of the ellipse:

$$\big(x_{\pm M'+\frac12,\pm N'+\frac12},y_{\pm M'+\frac12,\pm N'+\frac12}\big)=(\pm\ell,\pm h+0.5),$$

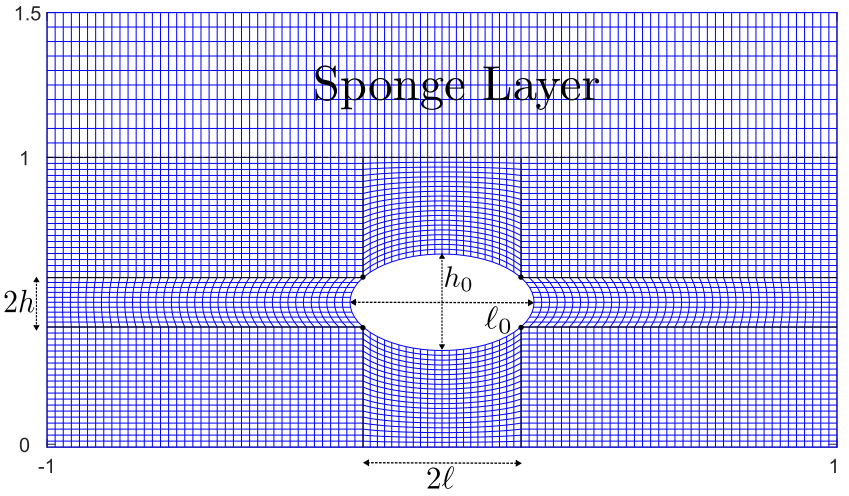

Fig. 3.3. Example 2: Structured quadrilateral mesh.

where $\ell < \ell_0/2$ and $h = h_0\sqrt{\frac{1}{4} - \frac{\ell^2}{\ell_0^2}}$; see Fig. 3.3. We then consider the cell vertices located below and above the zeppelin, that is, those vertices whose indices satisfy $|j| \le M'$ and $|k| \ge N'$; see Fig. 3.3. These cell vertices are given by

$$x_{j+\frac12,k+\frac12} = \tfrac{j\ell}{M'}, \quad j = -M', \dots, M',$$

$$y_{j+\frac12,k+\frac12} = \begin{cases} \frac{N+k}{N-N'}\left(\frac12 - h_0\sqrt{\frac14 - \frac{x^2_{j+\frac12,k+\frac12}}{\ell_0^2}}\right), & k = -N, \dots, -N', \\ 1 - \frac{N-k}{N-N'}\left(\frac12 - h_0\sqrt{\frac14 - \frac{x^2_{j+\frac12,k+\frac12}}{\ell_0^2}}\right), & k = N', \dots, N. \end{cases}$$

Similarly, the cell vertices located to the left and to the right of the zeppelin, that is, those vertices whose indices satisfy $|j| \ge M'$ and $|k| \le N'$, are given by

$$y_{j+\frac12,k+\frac12} = \tfrac{kh}{N'}, \quad k = -N', \dots, N',$$

$$x_{j+\frac12,k+\frac12} = \begin{cases} \frac{j+M'}{M-M'} - \frac{M+j}{M-M'}\cdot\ell_0\sqrt{\frac14 - \frac{y^2_{j+\frac12,k+\frac12}}{h_0^2}}, & j = -M, \dots, -M', \\ \frac{j-M'}{M-M'} + \frac{M-j}{M-M'}\cdot\ell_0\sqrt{\frac14 - \frac{y^2_{j+\frac12,k+\frac12}}{h_0^2}}, & j = M', \dots, M; \end{cases}$$

see Fig. 3.3. Next, the cell vertices in the four corners of the non-sponge part of the computational domain, that is, those whose indices satisfy $|j| > M'$ and $|k| > N'$, are

$$x_{j+\frac12,k+\frac12} = \begin{cases} \frac{j+M'}{M-M'} - \ell\frac{M+j}{M-M'}, & j = -M, \dots, -M'-1, \\ \frac{j-M'}{M-M'} + \ell\frac{M-j}{M-M'}, & j = M'+1, \dots, M, \end{cases}$$

$$y_{j+\frac12,k+\frac12} = \begin{cases} \frac{N+k}{N-N'}\left(\frac12 - h\right), & k = -N, \dots, -N'-1, \\ 1 - \frac{N-k}{N-N'}\left(\frac12 - h\right), & k = N'+1, \dots, N, \end{cases}$$

Finally, in the sponge layer $[-1, 1] \times [1, 1.5]$ we use a uniform mesh with

$$x_{j+\frac12,k+\frac12} = x_{j+\frac12,N+\frac12}, \quad j = -M, \dots, M,$$
$$y_{j+\frac12,k+\frac12} = 1 + \tfrac{k-N}{2N_s}, \quad k = N+1, \dots, N+N_s.$$

In the numerical simulations reported in Section 3.2.3, we have used $\ell = 0.2$. Notice that if ℓ is chosen to be close to either 0 or $\ell_0/2$, flat angles will appear in some of the cells, and this may cause numerical oscillations.

3.2.3. Results

We first compute the solution using the constructed mesh with $M = 400$, $N = 200$, $N_s = 50$, $M' = 81$ and $N' = 35$ until the final time $t = 33.55$ and plot the time snapshots of the obtained potential temperature θ in Fig. 3.4. At $t = 0$, the warm

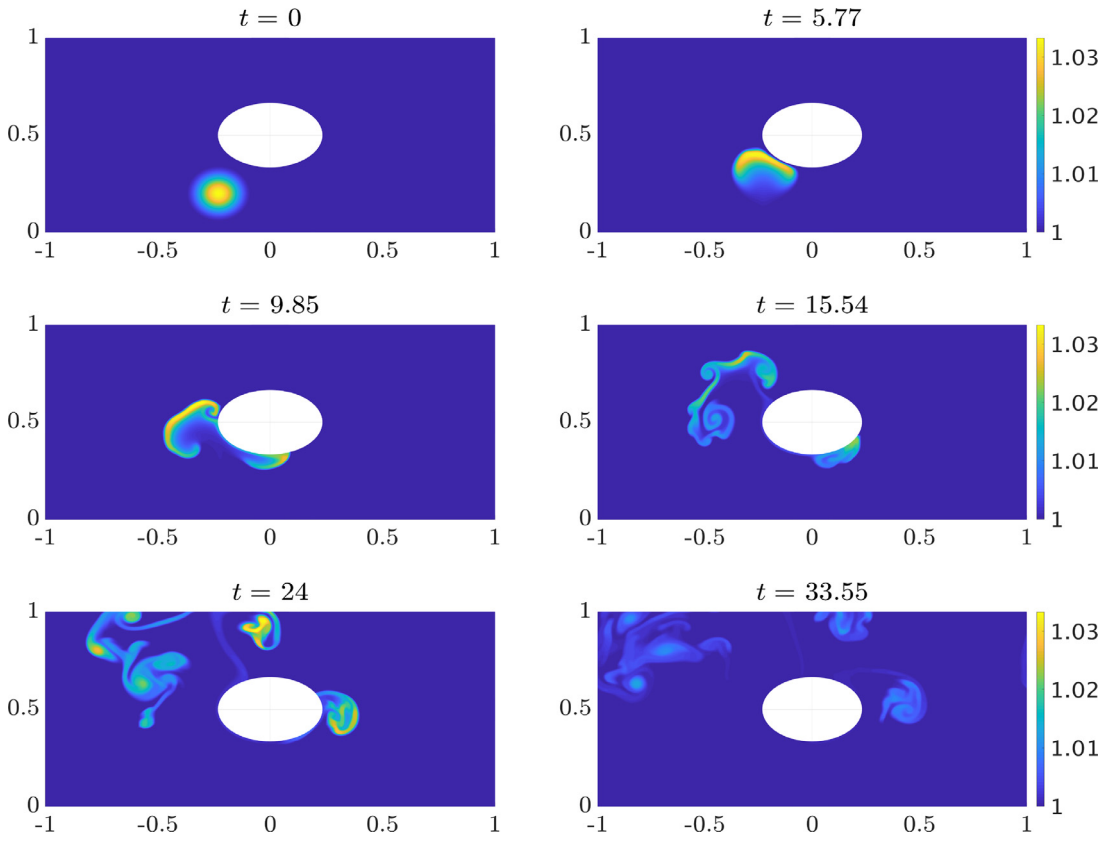

Fig. 3.5. Same as Fig. 3.4, but the results are computed using a finer mesh.

air circular area is located below the left part of the zeppelin. As a result of buoyancy effects, warm air rises and by the time $t = 5.77$ the warm air "bubble" touches the lower boundary of the zeppelin and then splits into two parts, which move along the surface of the zeppelin in the opposite directions. Later on, the left part of the "bubble" takes off the surface of the zeppelin, keeps rising and further splits into smaller pieces, while the right-going part of the "bubble" keeps sliding along the zeppelin. By the final time $t = 33.55$, the left part of the warm air spins counter-clockwise, the middle part spins clockwise and reaches the absorption layer, and the right part has detached from the zeppelin and started to rise and spin clockwise.

It should be observed that while the details of the warm air evolution are not the same as in the computations reported in Klein et al. [18], we find that the results are qualitatively similar. In order to further validate the proposed numerical method, we refine the mesh and compute the solution at the same sequence of times, but using $M = 800$, $N = 400$, $N_s = 100$, $M' = 161$ and $N' = 69$. The obtained results, plotted in Fig. 3.5, clearly demonstrate that the structure of the fine mesh solution is the same as the coarse mesh one, while, as expected, more small features are now resolved.

3.3. Example 3 (Lee waves)

In the final example taken from Durran [6], Gatti-Bono and Colella [9], Klein et al. [18], we test the capability of the proposed numerical method to accurately capture the Lee waves generated when gravitationally stratified flow passes a mountain. We take $g = 1.14$.

3.3.1. Problem settings

The computational domain is

$$\{(x, y) : -7.2 \le x \le 10.8,\ h(x) \le y \le 1.28\}, \quad h(x) = \frac{h_0 a^2}{x^2 + a^2}, \tag{3.2}$$

where $a = 1$ and $h_0 = 0.06$ represent the characteristic width and the height of the mountain. We set the solid wall boundary conditions on the top and the bottom of the computational domain, while the periodicity is imposed on the left and the right boundaries.

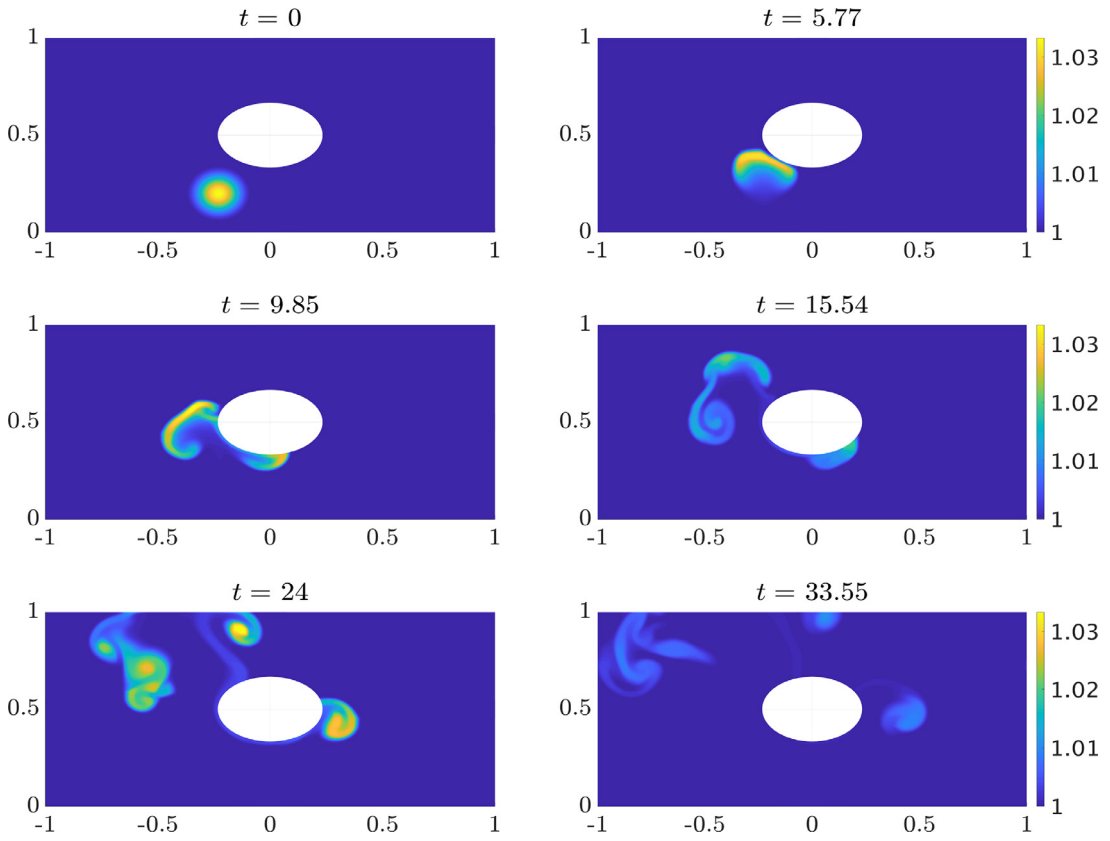

Fig. 3.4. Example 2: Potential temperature θ at different times.

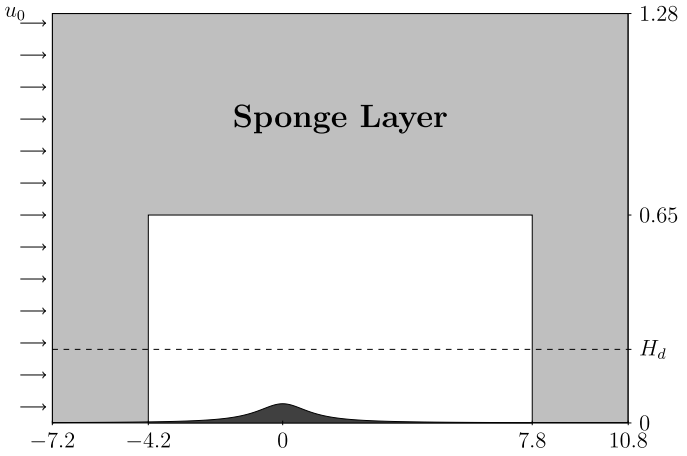

Fig. 3.6. Example 3: Computational domain.

A sponge layer is implemented to avoid gravity wave reflection from top of the domain and transmission across the horizontal boundaries. As illustrated in Fig. 3.6, the sponge width is 3 both on the left and on the right and its height is 0.63. In the sponge layer, we follow [18] and replace the computed solution at every stage of the SSP-RK3 method with the following relaxed values:

$$\bar{\boldsymbol{U}}^{\text{relax}}_{j,k} = \bar{\boldsymbol{U}}^{0}_{j,k} + \frac{1}{1+\Delta t\,\max\left(0.83\hat{x},\,0.17\hat{y}\right)}\left(\bar{\boldsymbol{U}}_{j,k} - \bar{\boldsymbol{U}}^{0}_{j,k}\right),$$

Table 3.2
Lee-wave parameters.

Parameter	Case (a)	Case (b)	Case (c)
H_d	0.1571	0.3142	0.3142
N_ℓ	0.6816	0.6816	0.3408
N_u	0.3408	0.3408	0.6816

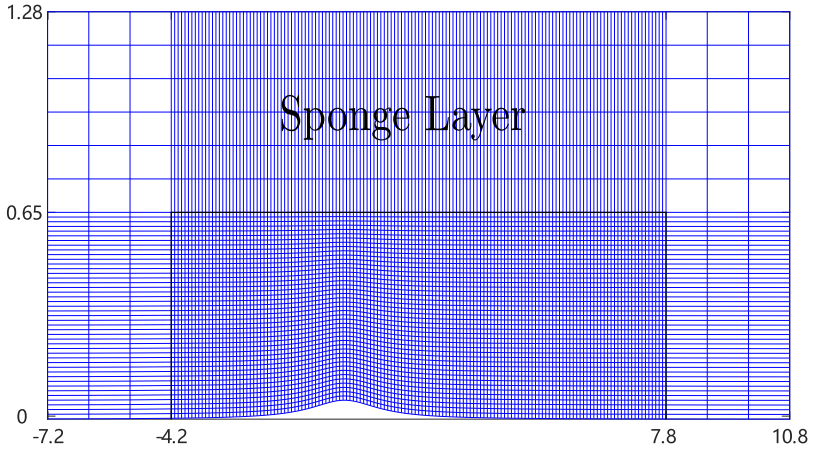

Fig. 3.7. Example 3: Structured quadrilateral mesh.

where $\bar{\boldsymbol{U}}^0_{j,k}$ are the initial data and $\hat{x}$ and $\hat{y}$ are the horizontal and vertical relative distances from the center of mass $(x_{j,k}, y_{j,k})$ of cell $C_{j,k}$ to the non-sponge part of the computational domain, namely, $\hat{x} := \max\big(x_{j,k} - 7.8, -4.2 - x_{j,k}, 0\big)$ and $\hat{y} := \max\big(y_{j,k} - 0.65, 0\big)$.

In this example, the steady-state solution satisfying (1.3) and (1.2) consists of two layers of atmosphere (with two different Brunt–Väisälä frequency constants N_ℓ and N_u for the lower and upper layers, respectively) separated at height H_d:

$$\theta_s(y) = \begin{cases} e^{N_\ell^2 y/g}, & y < H_d, \\ e^{[(N_\ell^2 - N_u^2)H_d + N_u^2 y]/g}, & y \geq H_d, \end{cases}$$

$$p_s(y) = \begin{cases} \left[1 - \frac{2g^2}{7N_\ell^2}\left(1 - e^{-N_\ell^2 y/g}\right)\right]^{7/2}, & y < H_d, \\ \left[p_{H_d}^{2/7} - \frac{2g^2}{7N_u^2} e^{-N_\ell^2 H_d/g}\left(1 - e^{-N_u^2(y-H_d)/g}\right)\right]^{7/2}, & y \geq H_d, \end{cases}$$

$$\rho_s(y) = \frac{[p_s(y)]^{5/7}}{\theta_s(y)},$$

where $p_{H_d} = \lim\limits_{y \to H_d^-} p_s(y) = \left[1 - \frac{2g^2}{7N_\ell^2}\left(1 - e^{-N_\ell^2 H_d/g}\right)\right]^{7/2}$. Similarly to Gatti-Bono and Colella [9], Klein et al. [18], we will consider three different combinations of parameters H_d, N_ℓ and N_u, given in Table 2.

We introduce the constant initial perturbation $u'(x, y, 0) = 0.06816$ in the horizontal velocity, while setting $v'(x, y, 0)$, $\rho'(x, y, 0)$ and $\theta'(x, y, 0)$ to be zero.

3.3.2. Mesh generation

The structured quadrilateral mesh we have used in this example is presented in Fig. 3.7.

This mesh is constructed as follows. We begin with the non-sponge part of the computational domain, which is

$$[x_{\min}, x_{\max}] \times [h(x), y_{\max}], \quad x_{\min} := -4.2, \quad x_{\max} := 7.8, \quad y_{\max} := 0.65,$$

where $h(x)$ is defined in (3.2). The cell vertices in this part of the domain are given by

$$x_{j+\frac{1}{2},k+\frac{1}{2}} = \left(1 - \tfrac{j}{M}\right)x_{\min} + \tfrac{j}{M}\, x_{\max}, \quad j = 0, \ldots, M,$$
$$y_{j+\frac{1}{2},k+\frac{1}{2}} = \left(1 - \tfrac{k}{N}\right)h\left(x_{j+\frac{1}{2},k+\frac{1}{2}}\right) + \tfrac{k}{N}\, y_{\max}, \quad k = 0, \ldots, N.$$

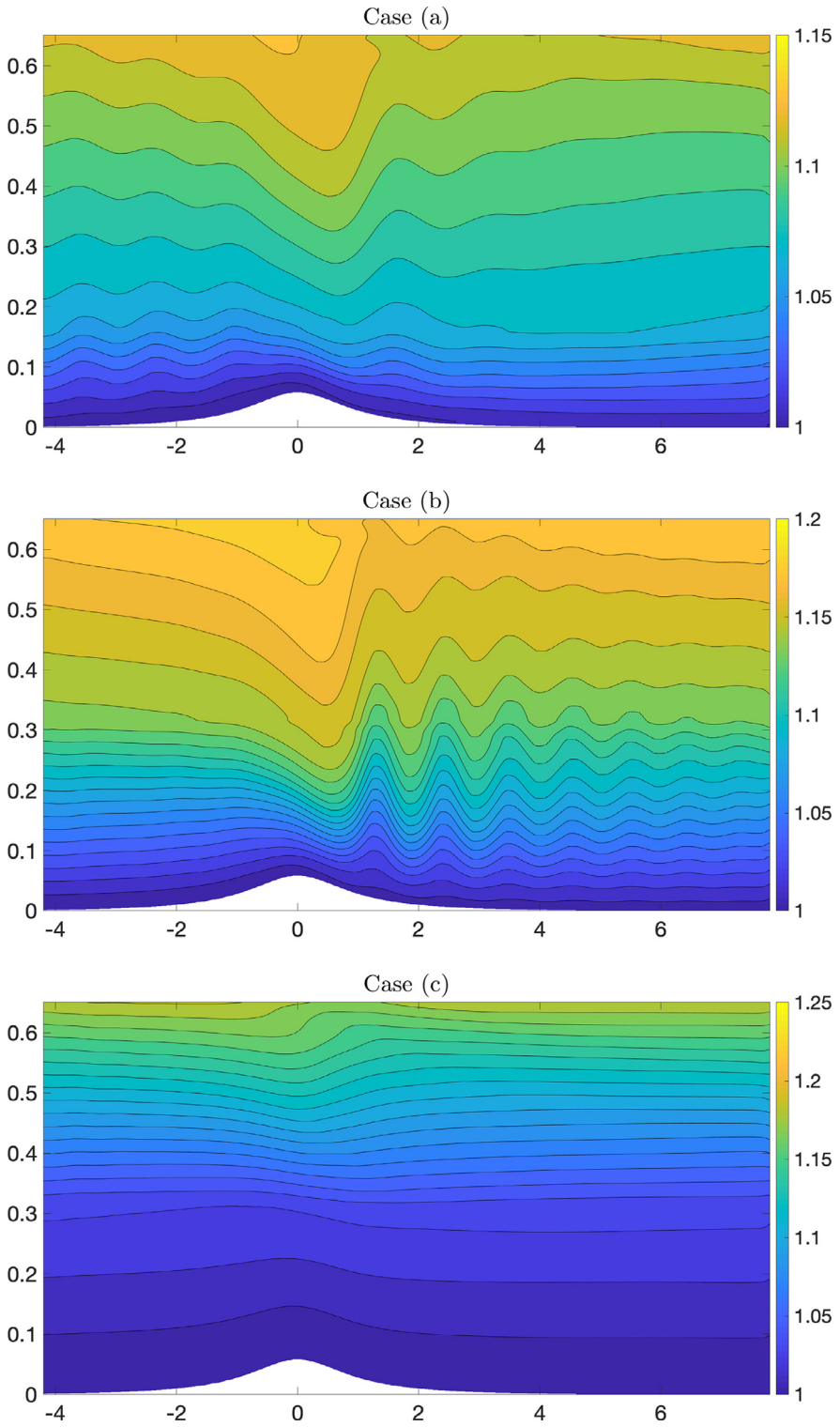

Fig. 3.8. Example 3: Potential temperature θ at $t = 293.4$ for Cases (a)–(c). Contours are plotted at intervals of $\Delta\theta = 0.01$.

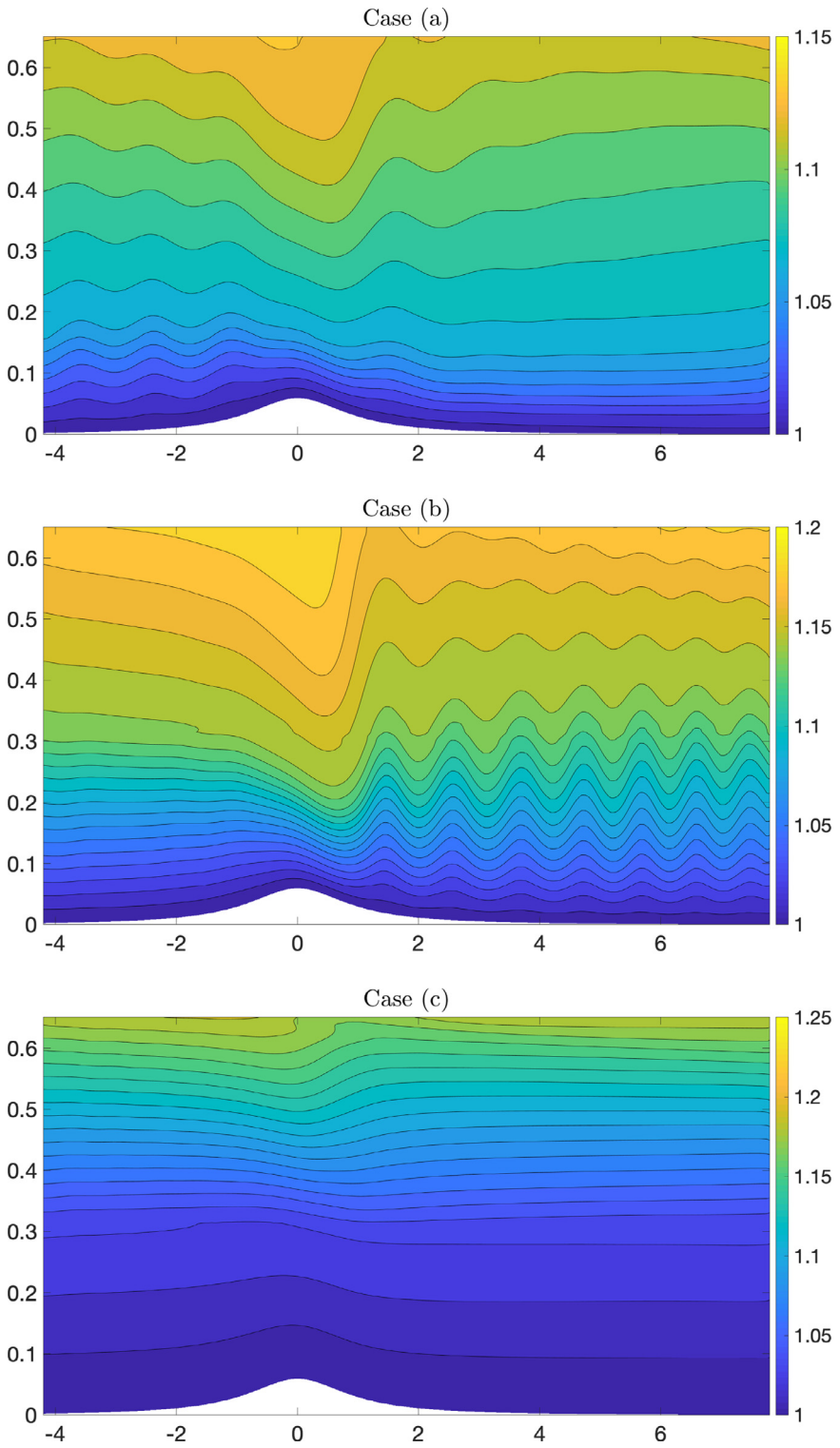

Fig. 3.9. Same as Fig. 3.8, but the results are computed using a finer mesh.

Within the sponge layer, we have

$$x_{j+\frac{1}{2},k+\frac{1}{2}} = \begin{cases} x_{\min} + \frac{j}{M_s} L_s, & j = -M_s, \dots, -1, \\ x_{\max} + \frac{j-M}{M_s} L_s, & j = M+1, \dots, M+M_s, \end{cases}$$

$$y_{j+\frac{1}{2},k+\frac{1}{2}} = \begin{cases} y_{j+\frac{1}{2},k+\frac{1}{2}} = \left(1 - \frac{k}{N}\right) h\left(x_{j+\frac{1}{2},k+\frac{1}{2}}\right) + \frac{k}{N} y_{\max}, & k = 0, \dots, N, \\ y_{\max} + \frac{k-N}{N_s} H_s, & k = N+1, \dots, N+N_s, \end{cases}$$

where $L_s = 3$ and $H_s = 0.63$.

3.3.3. Results

We first compute the solution using the constructed mesh with $M = 432$, $N = 132$, $M_s = 9$ and $N_s = 18$ until the final time $t = 293.4$ and plot the obtained potential temperature θ in Fig. 3.8. In all three Cases (a), (b) and (c), the results qualitatively match those reported in Durran [6], Gatti-Bono and Colella [9], Klein et al. [18]. We have also added the contour lines corresponding to different values of θ with the difference between adjacent contours being 0.01. As one can observe, in all of the three cases the "density" of contours changes at about $y = H_d$. One can also see more contours in the lower layer of atmosphere in Cases (a) and (b), while in Case (c) the situation is opposite: there are less contours in the lower layer. The location where the rate of potential temperature increase changes corresponds to the height of the interface between the two layers. It also indicates the place where turbulence occurs, which provides a useful information for practitioners studying the atmospheric dynamics. In addition, in Cases (a) and (b), one can observe a sharp drop of potential temperature above the downhill part ($0 \le x \le 2$). In Case (b), the occurrence of vertical oscillation of the perturbed air, which can be observed at about $x \in [1, 4]$, indicates the phenomenon of Lee waves. At the same time, in Cases (a) and (c), no significant change in gravity waves on the right of the mountain has been observed.

In order to further validate the proposed numerical method, we refine the mesh and compute the solution at the same final time, but using $M = 864$, $N = 264$, $M_s = 18$ and $N_s = 36$. The obtained results, plotted in Fig. 3.9, clearly demonstrate that the structure of the fine mesh solution is the same as the coarse mesh one, which experimentally indicates the convergence of the method.

Acknowledgments

The work of A. Chertock was supported in part by NSF grants DMS-1818684 and DMS-2208438. The work of A. Kurganov was supported in part by NSFC grants 12171226 and 12111530004, and by the fund of the Guangdong Provincial Key Laboratory of Computational Science and Material Design (No. 2019B030301001).

References

[1] M. Berger, C. Helzel, A simplified *h*-box method for embedded boundary grids, SIAM J. Sci. Comput. 34 (2) (2012) A861–A888.
[2] G. Bispen, M. Lukáčová-Medviďová, L. Yelash, Asymptotic preserving IMEX finite volume schemes for low Mach number Euler equations with gravitation, J. Comput. Phys. 335 (2017) 222–248.
[3] N. Botta, R. Klein, S. Langenberg, S. Lützenkirchen, Well balanced finite volume methods for nearly hydrostatic flows, J. Comput. Phys. 196 (2004) 539–565.
[4] P.T. Brady, D. Livescu, Foundations for high-order, conservative cut-cell methods: stable discretizations on degenerate meshes, J. Comput. Phys. (2020) 109794.
[5] A. Chertock, S. Cui, A. Kurganov, c. N. Özcan, E. Tadmor, Well-balanced schemes for the Euler equations with gravitation: conservative formulation using global fluxes, J. Comput. Phys. 358 (2018) 36–52.
[6] D.R. Durran, Another look at downslope windstorms. Part I: the development of analogs to supercritical flow in an infinitely deep, continuously stratified fluid, J. Atmos. Sci. 43 (1986) 2527–2543.
[7] E. Gaburro, M.J. Castro, M. Dumbser, Well-balanced arbitrary-Lagrangian–Eulerian finite volume schemes on moving nonconforming meshes for the Euler equations of gas dynamics with gravity, Mon. Not. R. Astron. Soc. 477 (2) (2018) 2251–2275.
[8] T. Gal-Chen, R.C.J. Somerville, On the use of a coordinate transformation for the solution of the Navier–Stokes equations, J. Comput. Phys. 17 (1975) 209–228.
[9] C. Gatti-Bono, P. Colella, An anelastic allspeed projection method for gravitationally stratfied flows, J. Comput. Phys. 216 (2006) 589–615.
[10] D. Ghosh, E.M. Constantinescu, Well-balanced, conservative finite difference algorithm for atmospheric flows, AIAA J. 54 (4) (2016) 1370–1385, doi:10.2514/1.J054580.
[11] F.X. Giraldo, M. Restelli, M. Läuter, Semi-implicit formulations of the Navier–Stokes equations: application to nonhydrostatic atmospheric modeling, SIAM J. Sci. Comput. 32 (6) (2010) 3394–3425, doi:10.1137/090775889.
[12] N. Gokhale, N. Nikiforakis, R. Klein, A dimensionally split Cartesian cut cell method for hyperbolic conservation laws, J. Comput. Phys. 364 (2018) 186–208.
[13] S. Gottlieb, D. Ketcheson, C.W. Shu, Strong Stability Preserving Runge–Kutta and Multistep time Discretizations, World Scientific Publishing Co. Pte. Ltd., Hackensack, NJ, 2011.
[14] S. Gottlieb, C.W. Shu, E. Tadmor, Strong stability-preserving high-order time discretization methods, SIAM Rev. 43 (1) (2001) 89–112. (electronic)
[15] L. Grosheintz-Laval, R. Käppeli, Well-balanced finite volume schemes for nearly steady adiabatic flows, J. Comput. Phys. 423 (2020) 109805,28, doi:10.1016/j.jcp.2020.109805.
[16] Z.I. Janji, On the pressure gradient force error in σ-coordinate spectral models, Mon. Wea. Rev. 117 (1989) 2285–2292.
[17] R. Käppeli, S. Mishra, A well-balanced finite volume scheme for the Euler equations with gravitation. the exact preservation of hydrostatic equilibrium with arbitrary entropy stratification, Astron. Astrophys. 587 (2016) A94.
[18] R. Klein, K.R. Bates, N. Nikiforakis, Well-balanced compressible cut-cell simulation of atmospheric flow, Philos. Trans. R. Soc. Lond. Ser. A 367 (1907) (2009) 4559–4575.

[19] C. Klingenberg, G. Puppo, M. Semplice, Arbitrary order finite volume well-balanced schemes for the Euler equations with gravity, SIAM J. Sci. Comput. 41 (2) (2019) A695–A721.
[20] A. Kurganov, C.T. Lin, On the reduction of numerical dissipation in central-upwind schemes, Commun. Comput. Phys. 2 (1) (2007) 141–163.
[21] A. Kurganov, Y. Liu, M. Lukáčová-Medviďová, A well-balanced asymptotic preserving scheme for the two-dimensional rotating shallow water equations with nonflat bottom topography, SIAM J. Sci. Comput. 44 (3) (2022) A1655–A1680.
[22] A. Kurganov, S. Noelle, G. Petrova, Semidiscrete central-upwind schemes for hyperbolic conservation laws and Hamilton–Jacobi equations, SIAM J. Sci. Comput. 23 (3) (2001) 707–740.
[23] A. Kurganov, M. Prugger, T. Wu, Second-order fully discrete central-upwind scheme for two-dimensional hyperbolic systems of conservation laws, SIAM J. Sci. Comput. 39 (3) (2017) A947–A965.
[24] A. Kurganov, Z. Qu, O. Rozanova, T. Wu, Adaptive moving mesh central-upwind schemes for hyperbolic system of PDEs. Applications to compressible Euler equations and granular hydrodynamics, Commun. Appl. Math. Comput. 3 (2021) 445–479.
[25] A. Kurganov, E. Tadmor, New high-resolution central schemes for nonlinear conservation laws and convection-diffusion equations, J. Comput. Phys. 160 (1) (2000) 241–282.
[26] R.J. LeVeque, A well-balanced path-integral f-wave method for hyperbolic problems with source terms, J. Sci. Comput. 48 (1–3) (2011) 209–226.
[27] P. Mittal, G. Iaccarino, Immersed boundary methods, Annu. Rev. Fluid Mech. 37 (2005) 239–261.
[28] N.A. Phillips, A coordinate system having some special advantages for numerical forecasting, J. Atmos. Sci. 14 (1957) 184–185.
[29] H. Shirkhani, A. Mohammadian, O. Seidou, A. Kurganov, A well-balanced positivity-preserving central-upwind scheme for shallow water equations on unstructured quadrilateral grids, Comput. Fluids 126 (2016) 25–40.
[30] A.J. Simmons, D.M. Burridge, An energy and angular-momentum conserving vertical finite-difference scheme and hybrid vertical coordinates, Mon. Wea. Rev. 109 (1981) 758–766.
[31] H. Sundqvist, On vertical interpolation and truncation in connexion with use of sigma system models, Atmosphere 14 (1976) 37–52.
[32] K. Wu, Y. Xing, Uniformly high-order structure-preserving discontinuous Galerkin methods for Euler equations with gravitation: positivity and well-balancedness, SIAM J. Sci. Comput. 43 (1) (2021) A472–A510, doi:10.1137/20M133782X.
[33] Y. Xing, C.W. Shu, High order well-balanced WENO scheme for the gas dynamics equations under gravitational fields, J. Sci. Comput. 54 (2013) 645–662.
[34] L. Yelash, A. Müller, M. Lukáčová-Medvid'ová, F.X. Giraldo, V. Wirth, Adaptive discontinuous evolution Galerkin method for dry atmospheric flow, J. Comput. Phys. 268 (2014) 106–133, doi:10.1016/j.jcp.2014.02.034.